OXFORD

SOT | Society of Toxicology
www.toxsci.oxfordjournals.org

TOXICOLOGICAL SCIENCES, 170(2), 2019, 330–344

doi: 10.1093/toxsci/kfz096
Dryad Digital Repository DOI: https://doi.org/10.5061/dryad.7c7b561
Advance Access Publication Date: April 17, 2019
Research Article

TSPO PET Using [^{18}F]PBR111 Reveals Persistent Neuroinflammation Following Acute Diisopropylfluorophosphate Intoxication in the Rat

Brad A. Hobson,[*] Douglas J. Rowland,[†] Sílvia Sisó,[‡] Michelle A. Guignet,[§] Zachary T. Harmany,[†] Suren B. Bandara,[§] Naomi Saito,[¶] Danielle J. Harvey,[¶] Donald A. Bruun,[§] Joel R. Garbow,[‖] Abhijit J. Chaudhari,[*,†] and Pamela J. Lein[§,1]

[*]Department of Radiology, University of California Davis School of Medicine, Sacramento, California 95817; [†]Center for Molecular and Genomic Imaging, Department of Biomedical Engineering, University of California Davis College of Engineering, Davis, California 95616; [‡]Department of Pathology, Microbiology and Immunology; [§]Department of Molecular Biosciences, University of California Davis School of Veterinary Medicine, Davis, California 95616; [¶]Department of Public Health Sciences, University of California Davis School of Medicine, Davis, California 95616; and [‖]Department of Radiology, Washington University in St. Louis, St. Louis, Missouri 63110

[1]To whom correspondence should be addressed at Department of Molecular Biosciences, University of California Davis School of Veterinary Medicine, 1089 Veterinary Medicine Drive, Davis, CA 95618. Fax: (530) 752-7690; E-mail:pjlein@ucdavis.edu.

ABSTRACT

Acute intoxication with organophosphates (OPs) can trigger status epilepticus followed by persistent cognitive impairment and/or electroencephalographic abnormalities. Neuroinflammation is widely posited to influence these persistent neurological consequences. However, testing this hypothesis has been challenging, in part because traditional biometrics preclude longitudinal measures of neuroinflammation within the same animal. Therefore, we evaluated the performance of noninvasive positron emission tomography (PET), using the translocator protein (TSPO) radioligand [^{18}F]PBR111 against classic histopathologic measures of neuroinflammation in a preclinical model of acute intoxication with the OP diisopropylfluorophosphate (DFP). Adult male Sprague Dawley rats administered pyridostigmine bromide (0.1 mg/kg, im) 30 min prior to administration of DFP (4 mg/kg, sc), atropine sulfate (2 mg/kg, im) and 2-pralidoxime (25 mg/kg, im) exhibited moderate-to-severe seizure behavior. TSPO PET performed prior to DFP exposure and at 3, 7, 14, 21, and 28 days postexposure revealed distinct lesions, as defined by increased standardized uptake values (SUV). Increased SUV showed high spatial correspondence to immunohistochemical evidence of neuroinflammation, which was corroborated by cytokine gene and protein expression. Regional SUV metrics varied spatiotemporally with days postexposure and correlated with the degree of neuroinflammation detected immunohistochemically. Furthermore, SUV metrics were highly correlated with seizure severity, suggesting that early termination of OP-induced seizures may be critical for attenuating subsequent neuroinflammatory responses. Normalization of SUV values to a cerebellar reference region improved correlations to all outcome measures and seizure severity. Collectively, these results establish TSPO PET using [^{18}F]PBR111 as a robust, noninvasive tool for longitudinal monitoring of neuroinflammation following acute OP intoxication.

Key words: diisopropylfluorophosphate; GFAP; IBA1; *in vivo* imaging; positron emission tomography; organophosphate; neuroinflammation; TSPO.

Acute poisoning with cholinesterase-inhibiting organophosphorus (OPs) pesticides and nerve agents is a serious public health problem, with the worldwide incidence estimated at 1 million intoxications and 200,000 deaths annually (Gunnell *et al.*, 2007; Mew *et al.*, 2017). Acute OP intoxication can cause cholinergic crisis and seizures, and survivors often face debilitating, long-term morbidity in the form of delayed onset epilepsy, cognitive dysfunction, changes in brain structure, and encephalopathies (Aroniadou-Anderjaska *et al.*, 2016; Chen, 2012; Pereira *et al.*, 2014). The mechanisms underlying these long-term consequences are poorly understood.

Neuroinflammation is proposed as a mechanism contributing to the development of long-term consequences following acute OP intoxication (Chen, 2012; Collombet, 2011; de Araujo Furtado *et al.*, 2012; Guignet and Lein, 2019). Preclinical studies of acute OP intoxication reveal a robust neuroinflammatory response that develops before the onset of long-term morbidity and persists for weeks to months. (Aroniadou-Anderjaska *et al.*, 2016; Chen, 2012; Collombet, 2011; Flannery *et al.*, 2016; Rojas *et al.*, 2016). This prolonged neuroinflammation is characterized by region-specific proinflammatory cytokine release (Johnson *et al.*, 2011), inflammatory gene expression (Spradling *et al.*, 2011), and gliosis (Collombet *et al.*, 2005; Flannery *et al.*, 2016), with gliosis being the most consistently observed of these neuroinflammatory responses (Chapman *et al.*, 2015; Guignet and Lein, 2019). Attenuation of OP-induced neuroinflammation appears to mitigate some behavioral deficits (Ferrara-Bowens *et al.*, 2017; Rojas *et al.*, 2016), suggesting neuroinflammation may be mechanistically relevant. However, these studies did not assess neuroinflammation prior to the manifestation of long-term consequences.

Monitoring neuroinflammation during the evolution of clinically relevant sequelae has been challenging because of considerable interanimal variability following acute OP intoxication (de Araujo Furtado *et al.*, 2010; Flannery *et al.*, 2016; Gullapalli *et al.*, 2010; Siso *et al.*, 2017). Moreover, traditional histological approaches preclude repeated, longitudinal assessments in the same animal. Because of these technical challenges, questions regarding relationships between the progression of neuroinflammation and the development of persistent morbidity remain largely unanswered.

In vivo imaging of the translocator protein (TSPO) via positron emission tomography (PET) may enable noninvasive collection of information regarding the extent, severity, and progression of neuroinflammatory responses across the whole brain following acute OP intoxication. TSPO is an 18-kDa transport protein located on the outer mitochondrial membrane that functions in cholesterol transport and steroid synthesis (Bonsack and Sukumari-Ramesh, 2018). Under physiologic conditions, TSPO expression in the brain is low and localized to endothelial and Purkinge cells (Betlazar *et al.*, 2018); however, during an inflammatory response, TSPO is significantly upregulated in microglia and astrocytes, but not neurons (Guilarte, 2018). TSPO PET has been used to monitor neuroinflammation in numerous preclinical models and clinical cases of neurologic disease and injury (Dupont *et al.*, 2017; Owen and Matthews, 2011), including epilepsy (Bertoglio *et al.*, 2017). These studies have demonstrated that the contribution of different cell types to the TSPO PET signal can vary widely across diseases and models (Lavisse *et al.*, 2012; Nguyen *et al.*, 2018; Weidner *et al.*, 2018; Yamasaki *et al.*, 2017), highlighting the need to validate TSPO PET data to histological characterization neuroinflammation in individual models. There are currently no data evaluating the correspondence of TSPO PET imaging to histologic indices of neuroinflammation in any model of acute OP intoxication.

We previously demonstrated the technical feasibility of TSPO PET using the [^{11}C]PK11195 radiotracer (Flannery *et al.*, 2016) in an established rat model of acute OP intoxication using diisopropylfluorophosphate (DFP) (Deshpande *et al.*, 2010; Hobson *et al.*, 2017; Pouliot *et al.*, 2016; Siso *et al.*, 2017). TSPO PET indicated an increase in [^{11}C]PK11195 uptake during the first 21 days postintoxication, suggesting persistent neuroinflammation (Flannery *et al.*, 2016). However, that study utilized a first generation ^{11}C-based TSPO radiotracer known to have low brain permeability, high nonspecific and plasma protein binding, and consequently low signal-to-noise ratio in PET images, and limited clinical relevance (Vivash and O'Brien, 2016). Importantly, the study design precluded time-matched histologic characterization of neuroinflammatory responses in the small cohort of imaged animals (Flannery *et al.*, 2016). To address these limitations, we performed TSPO PET using [^{18}F]PBR111, a second generation radioligand for TSPO (Fookes *et al.*, 2008) with lower nonspecific binding, improved binding potential, and lower fraction of radiometabolites than [^{11}C]PK11195 (Van Camp *et al.*, 2010), and quantified histologic measures of neuroinflammation in imaged animals. Our findings demonstrate that [^{18}F]PBR111 PET detects significant microgliosis and astrogliosis that correspond spatiotemporally to histologic evidence of these neuroinflammatory responses. These findings establish the feasibility of using TSPO PET imaging for longitudinal monitoring of neuroinflammation in the rat model of acute DFP intoxication.

MATERIALS AND METHODS

Animals and DFP exposure. Animals were maintained in facilities fully accredited by the Association for Assessment and Accreditation of Laboratory Animal Care, and all studies were performed with regard to the alleviation of pain and suffering under protocols approved by the UC Davis Institutional Animal Care and Use Committee. Adult male Sprague Dawley rats (250–280 g; Charles River Laboratories, Hollister, California) were housed individually in standard plastic cages under controlled environmental conditions (22°C ± 2°C, 40%–50% humidity) with a normal 12-h light/dark cycle. Food and water were provided *ad libitum*. As illustrated in a schematic of the acute DFP intoxication model (Figure 1), unanesthetized rats were administered DFP (90% ± 7% as determined by [^{1}H]-NMR, Sigma Chemical Company, St Louis, Missouri) at 4 mg/kg, sc, as described previously (Hobson *et al.*, 2017; Siso *et al.*, 2017). DFP was diluted into sterile ice-cold 0.2 M phosphate buffered saline (PBS) (150 mM NaCl, pH 7.2). Vehicle (VEH) control animals received an equivalent injection volume of ice-cold PBS. DFP-exposed and VEH control animals were pretreated with pyridostigmine bromide (PB) (purity >98.0%, TCI America, Portland, Oregon) in saline at 0.1 mg/kg, im, 30 min prior to DFP. Immediately following DFP exposure, DFP and VEH animals were administered atropine

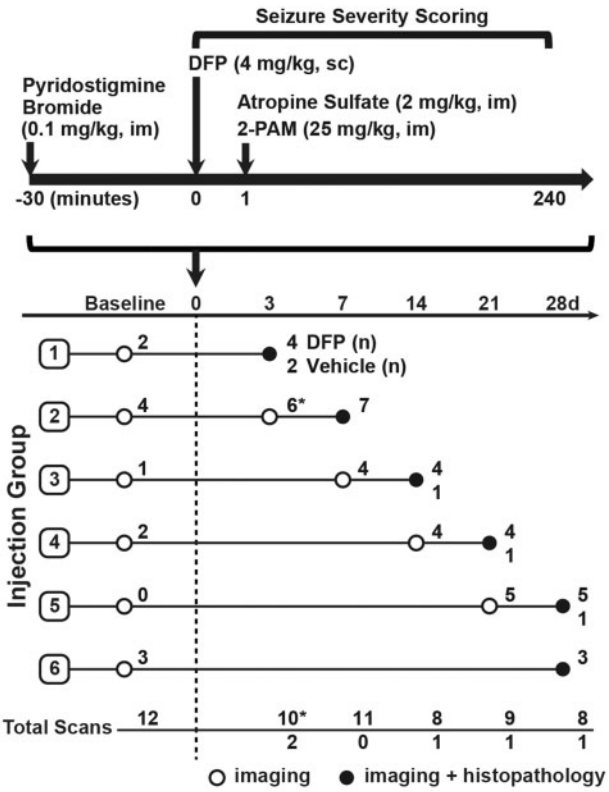

Figure 1. Schematic illustrating the DFP exposure paradigm and experimental design of imaging studies, adapted from (Hobson *et al.*, 2017). Imaging and histopathological examinations were performed on 27 DFP-exposed and 5 VEH control rats at varying days postexposure (DPE). The number of DFP-injected animals (DFP) and VEH controls imaged per time point is listed at the end of each row. Asterisks at the day 3 imaging time point denote a technical error during image acquisition that resulted in dramatically reduced SUV values in 6 animals (Supplementary Figure 1). These scans were excluded during temporal modeling analysis. Note that subsets of animals were imaged at 1–7 days prior to DFP exposure (baseline).

sulfate (purity ≥97%, Sigma Chemical Company) at 2.0 mg/kg, im, and 2-pralidoxime (2-PAM, purity ≥97%, Sigma Chemical Company) at 25 mg/kg in saline, im. These drugs significantly reduce mortality by effectively blocking the peripheral parasympathomimetic symptoms associated with acute OP intoxication (Kim *et al.*, 1999). At 6 h postexposure, animals were injected, sc, with 10 ml of 5% dextrose in saline (Baxter, Deerfield, Illinois) and returned to their home cages. Rats were provided a mixture of powdered rat chow in water for 3–5 days until they were able to locate and consume standard chow and water.

The severity of seizure behavior was quantified using a 6-point scale (Table 1) as previously described (Deshpande *et al.*, 2010; Hobson *et al.*, 2017; Siso *et al.*, 2017). Briefly, seizure behavior was scored at 5 min intervals from 0 to 120 min postDFP injection, and at 20 min intervals from 120 to 240 min postDFP injection. Seizure severity was quantified as the average seizure severity score (SS_{AVR}) based on ≥ 16 observations during the initial 4 h postDFP.

In vivo *imaging and analysis*. Animals were imaged at 1–3 time points, ranging from 7 days prior to DFP or VEH injection out to 28 d postDFP or VEH exposure (Figure 1). At the time of imaging, animals were anesthetized with isoflurane/O_2 (Piramal Healthcare, Bethlehem, Pennsylvania) using 2.0%–3.0% vol/vol

Table 1. Scale for Scoring Seizure Severity

Score	Behavior
0	No signs or symptoms
1	SLUD
2	Muscle fasciculations, tremors
3	Forelimb clonus
4	Rearing, hindlimb clonus
5	Rearing and falling, loss of righting reflex

Abbreviation: SLUD: salivation, urination, lacrimation, and defecation.

to induce and 1.0%–2.0% vol/vol to maintain anesthesia. Once anesthetized, animals were restrained in a stereotaxic apparatus, and imaged for up to 1 h for PET and 2 h for magnetic resonance imaging (MRI) (protocols described below). During this time, the animal's body temperature was maintained at 37°C using warm air or a heat lamp, and anesthesia was adjusted to maintain a respiration rate of 50–70 breaths per minute.

Magnetic resonance imaging. For anatomic reference, magnetic resonance (MR) images were acquired using a 7T preclinical MR scanner (Bruker BioSpin MRI, Ettlingen Germany) equipped with a 116-mm internal diameter B-GA12S gradient (450 mT/m, 4500 T/m/s), a 72-mm internal diameter linear transmit coil, and a 4-channel, rat-brain phased array in cross-coil configuration for signal reception. T_2-weighted, fast spin echo (Rapid Acquisition with Repeated Echoes, RARE) transaxial images were collected over 10 min using the following parameters: repetition time = 6100 ms; echo time = 15 ms; echo train length (RARE factor) = 8; averages = 4; field of view = 35 × 25 mm^2 with an in-plane data matrix of 280 × 200, resulting in a data set resolution of 0.125 × 0.125 mm^2; and 44 slices with a 0.5-mm thickness, spanning approximately 7.5 to −13.5 mm bregma. Images were acquired and reconstructed using Paravision 5.1 (Bruker BioSpin, MRI). T2-weighted image data can be found in the Dryad Digital Repository (doi:10.5061/dryad.7c7b561). Diffusion tensor imaging (DTI) data were also acquired, utilizing the remaining MR scan time. DTI data are the subject of a previous publication (Hobson *et al.*, 2017) and, therefore, will not be discussed further in this article.

Image segmentation of sequential MR images was performed using manual delineation tools in PMOD v4.0 (PMOD Technologies, Zurich, CHE). Volumes of interest (VOIs) definitions (bilateral brain regions) were guided by Paxinos and Watson's *The Rat Brain in Stereotaxic Coordinates* (Paxinos and Watson, 2007). The axial extent of brain-region VOIs, listed as "distance from bregma"/"extent in mm", were: amygdala, −1.5/2.5 cerebellum, −11.0/2.0; hippocampus, −2.5/3.5; piriform cortex, 2.0/5.0; and thalamus, −1.5/2.5.

Positron emission tomography. Automated synthesis of [^{18}F]PBR111 was performed according to previously described methods (Bourdier *et al.*, 2012), achieving a mean-specific activity of 643.95 PBq/mol over 23 productions. Animals were imaged with 1 of 2 preclinical PET systems (Inveon Dedicated PET; or microPET Focus 120; both Siemens Medical Solutions, Knoxville, Tennessee). Each animal was imaged on the same scanner at the various time points. Immediately after the start of data acquisition, a bolus of [^{18}F]PBR111 was delivered by tail-vein injection at an average activity concentration of 39.6 ± 2.2 MBq in 200 μl saline. The scan duration was 60 min. PET data were reconstructed using 2 iterations of the 3D ordered subset expectation maximization method followed by 18 iterations of a

maximum a posteriori algorithm into 2 frames with the second being used for SUV calculations (1200 and 2400 s). The imaging matrix was 128 × 128 × 95 with reconstructed voxel sizes of 0.43 × 0.43 × 0.80 mm.

PET images were coregistered to MRI using PMOD v4.0 (PMOD Technologies) and the standardized uptake value (SUV) and SUV normalized to a cerebellar reference region (SUVR) were calculated for each VOI according to equations 1 and 2, respectively:

$$\mathrm{SUV}(t) = \frac{C(t)}{\mathrm{ID}/\mathrm{BW}} \quad (1)$$

$$\mathrm{SUVR}(t) = \frac{C_{\mathrm{VOI}}(t)}{C_{\mathrm{Reference}}(t)} \quad (2)$$

in which C is the mean tissue activity concentrations in MBq/ml at time t, ID is the injected dose in MBq, and BW is body weight in grams at the time of scanning. VOI mean activity concentrations were extracted from an average of the final 2400 s of data collection (1200 - 3600 s). Selection of the final 2400 s of data collection for data analysis was based on visual inspection of VOI time activity curves and a previous publication (Dedeurwaerdere *et al.*, 2012), suggesting [^{18}F]PBR111 uptake remains stable during this time.

Histology. A detailed description of how samples used in this study were prepared for histologic assessment has been previously published (Siso *et al.*, 2017). Briefly, brains were harvested at 3, 7, 14, 21, or 28 days postexposure (DPE) from animals deeply anesthetized with 4% isoflurane in oxygen and subsequently perfused transcardially with cold 0.2 M PBS (3.6 mM Na_2HPO_4, 1.4 mM NaH_2PO_4, 150 mM NaCl, pH 7.2) followed by cold 4% paraformaldehyde (Sigma Chemical Company) in 0.2 M phosphate buffer. After 1-week postfixation in 4% paraformaldehyde, brains were paraffin-embedded, sliced into 5-micron thick sections, mounted and immunostained for glial fibrillary acidic protein (GFAP, 1:600, Z0334, Dako North America, Carpinteria, California) or ionized calcium-binding adaptor molecule (IBA1, 1:600, 19-19741, Wako, Richmond, Virginia) to assess astrogliosis and microgliosis, respectively.

A veterinary neuropathologist blinded to treatment inspected tissue sections at multiple mm bregma per animal at magnifications ranging from 40× to 600× magnification to characterize neuroinflammation as identified by IBA1 or GFAP immunoreactivity (Siso *et al.*, 2017). Microgliosis was scored based on the following characteristics: increased density of IBA1 positive cells consistent with the appearance of histiocytes, morphological evidence of microglial activation as indicated by an ameboid shape (Perry *et al.*, 2010), and neuronophagia by ameboid microglia. Astrogliosis was scored based on the following characteristics: increased intensity of GFAP immunoreactivity in cells whose morphology was consistent with that of astrocytes, increased density of GFAP immunopositive astrocytes, and morphological evidence of astrocytic activation as indicated by swollen soma and thicker, shorter processes. Regional microgliosis and astrogliosis were scored in 0.5 increments using a scale ranging from 0 to 3 with 0 indicating no evidence of gliosis; 1, focal distribution of gliosis; 2, multifocal distribution of gliosis; and 3, segmental distribution of gliosis. Overall neuroinflammation was assessed using a "total neuroinflammation" score, defined as the sum of scores for astrogliosis and microgliosis within a single brain region.

Multiplex bead array immunoassay of cytokines and chemokines. A cohort of animals not used for imaging studies were dosed with either DFP (4 mg/kg, sc) or an equivalent volume of VEH (300 μl PBS, sc) followed 1 min later by coinjection of atropine sulfate (2 mg/kg, im) and 2-PAM (25 mg/kg, im). At 1, 3, 7, 14, or 28 DPE, animals were deeply anesthetized with 4% isoflurane in oxygen and subsequently perfused with cold PBS (3.6 mM Na_2HPO_4, 1.4 mM NaH_2PO_4, and 150 mM NaCl, pH 7.2). Brains were then extracted, the hippocampus and piriform cortex rapidly dissected out on ice, flash frozen on dry ice and stored at −80°C until further processed for protein levels of cytokines using a multiplex bead array immunoassay.

One difference between the cohort of animals used for these studies versus those used for TSPO PET imaging followed by collection of brain tissue for histologic assessment was that the animals used for imaging were administered PB 30 min prior to injection of DFP or VEH whereas the animals used for cytokine analyses were not pretreated with PB. We recently demonstrated that PB pretreatment had no effect on acetylcholinesterase inhibition, seizure behavior, or survival in the rat model of acute DFP intoxication (Bruun *et al.*, 2019). To confirm that PB pretreatment did not influence expression of inflammatory cytokines and chemokines following acute DFP intoxication, we collected additional samples from a small cohort of DFP animals that were administered PB (0.1 mg/kg, im) 30 min prior to DFP or VEH with subsequent atropine and 2-PAM. These animals were euthanized at 1 or 7 DPE, and the hippocampus was dissected, flash frozen and stored at −80°C.

For the immunoassay, approximately 500 mg of frozen tissue was washed in cell wash buffer and homogenized in 200 μl of lysing solution (Bio-Plex Cell Lysis Kit, Bio-Rad, Hercules, California) containing cOmplete Protease Inhibitor Cocktail (Sigma Aldrich, St Louis, Missouri) according to the manufacturer's instructions. Total protein content in the tissue lysate was determined using Pierce BCA Protein Kit Assay (ThermoFisher Scientific, Waltham, Massachusetts), and 150 μg of total protein was diluted in 50 μl of cell lysing solution and added to each well of the immunoassay plate. Cytokines were quantified following the manufacturer's instructions using Bio-Plex Pro Rat Cytokine 23 Plex Assay (Bio-Rad) containing interleukin (IL)-1α, IL-1β, IL-2, IL-4, IL-5, IL-6, IL-7, IL-10, IL-12(p70), IL-13, IL-17, IL-18, chemokine (C-X-C motif) ligand 1 (CXCL1 [GRO/KC]), macrophage inflammatory protein (MIP)-1a (CCL3), MIP-3a (CCL20), chemokine (C-C motif) ligand 5 (CCL5 [RANTES]), vascular endothelial growth factor (VEGF), monocyte chemoattractant protein 1 (MCP-1 [CCL2]), granulocyte colony-stimulating factor (G-CSF), granulocyte-macrophage CSF (GM-CSF), macrophage CSF (M-CSF), interferon (IFN)-γ, and tumor necrosis factor (TNF)-α. The bead sets were analyzed using a flow-based Luminex 100 suspension array system (Bio-Plex 200; Bio-Rad) and all sample concentrations were calculated using Bio-Plex Manager software. A 5-parameter model based on the known reference cytokine concentrations supplied by the manufacturer was used to calculate final concentrations; all values are expressed in pg/ml.

Reverse transcription quantitative polymerase chain reaction. Total RNA was purified from rat hippocampal tissues in a subset of the animals used for cytokine analysis using a hybrid method with TRIzol Reagent (ThermoFisher Scientific) and RNeasy Mini Kit (Qiagen, Hilden, Germany). Approximately 100 mg of frozen tissue was homogenized in 1 ml of TRIzol reagent and allowed to sit on ice for 5 min before adding 200 μl of chloroform. The tissue homogenate was centrifuged at 12 000 × g for 15 min at 4°C. The aqueous phase was collected, transferred to an RNeasy

Mini kit column, and further processed according to the manufacturer's instructions. Purified RNA was then reverse transcribed using the high capacity cDNA transcription kit (ThermoFisher Scientific) according to the manufacturer's instructions. Real time PCR was performed in 12.25 μl reactions containing 1 μl nuclease free water, 6 μl POWER SYBR Green PCR Master Mix (ThermoFisher Scientific), 0.2 μM primers, and 5 μl of cDNA. Samples were amplified using an Applied Biosystems 7900HT Fast thermocycler (available through the Real-Time PCR Research and Diagnostics Core Facility at UC Davis). PCR conditions for *IL-1β, TNF-α, IL-10*, and *CCL2 (MCP-1)* were: 50°C for 2 min, 95°C for 10 min, and then 40 cycles of 95°C for 15 s, 60°C for 30 s, and 72°C for 30 s. Conditions for *IL-6* and *IFN-γ* had the same starting steps, except the 40 cycles were conducted at 95°C for 15 s, 62°C for 30 s, and 72°C for 30 s.

Primer sets were designed in-house and tested for specificity using Primer-BLAST searches against nucleotide collection databases for *Rattus Norvegicus* and were synthesized by IDT (Coralville, Iowa) as previously described (Stamou *et al.*, 2014). Sequences of the primers used for *IL-1β*: (forward) 5′-GACTTCAC CATGGAACCCGT-3′ and (reverse) 5′-GGAGACTGCCCAT TCTCGAC-3′; *TNF-α:* (forward) 5′-CAGCAGATGGGCTGTACCTT-3′ and (reverse) 5′-AAATGGCAAATCGGCTGACG-3′; *IL-6* (forward) 5′-CTGGTCTTCTGGAGTTCCGT-3′ and (revers) 5′- TGCTCTGA ATGACTCTGGCT-3′; *IFN-γ* (forward) 5′-GTGTCATCGAATC GCACCTG-3′ and (reverse) 5′-GTTCACCTCGAACTTGGCGA-3′; *IL-10*: (forward) 5′-TTGAACCACCCGGCATCTAC-3′ and (reverse) 5′-CCAAGGAGTTGCTCCCGTTA-3′; *CCL2 (MCP-1)* (forward) 5′-CTTCCTCCACCACTATGCAGG-3′ and (reverse) 5′-GATGCTAC AGGCAGCAACTG-3′. Commercially available primer sequences were used for the 2 reference genes: (1) peptidylprolyl isomerase a (*Ppia)* (forward) 5′-ATCAGCCGTGATGTCGAAG-3′ and (reverse) 5′-TTTGCAGACGCCGCTGT-3′, (2) hypoxanthine-guanine phosphoribosyl transferase (*HPRT*) (forward) 5′-GCTTTTCCACTTT CGCTGATG-3′ and (reverse) 5′-GGTGAAAAGGACCTCTCGAAG-3′. Relative mRNA abundance was determined by the REST method as previously described (Pfaffl *et al.*, 2002) normalizing to the geometric mean of *Ppia* and *HPRT* reference genes.

Statistical analysis. All statistical analyses were performed in SAS (version 9.4, SAS Institute, Inc., Cary, North Carolina) and GraphPad Prism (version 7.03 GraphPad Software, Inc, San Diego, California). Results with p values $< .05$ were considered significant. Mixed-effects regression models were used to evaluate differences in regional PET metrics across varying time points postexposure, accounting for the repeated measures across brain regions (all animals) and time (where appropriate for animals receiving repeated imaging). To meet the assumption of constant variance, both PET metrics were transformed using the natural log prior to analysis. Factors of interest included brain region and time, as well as their interaction. All models included animal-specific random intercepts to account for the repeated measures within animals. Contrasts were defined to test for differences between preexposure/VEH values and postexposure values at specific time points. Wald tests were used to test for differences. Models were run with and without observations from 6 animals, all scanned in the same session on day 3, with SUV values across all brain regions that were atypical of the other animals due to a technical error (Supplementary Figure 1). Results were similar between the 2 models and models without these observations are presented for clarity.

The PET metrics, SUV and SUVR, were correlated to histopathological scoring and seizure severity using Spearman correlation. Correlations with histology utilized the final imaging time point of all DFP-exposed animals (27/27) and VEH animals (5/5). PET metrics and histopathological findings from VEH control animals were uniform across the 28-day study and, therefore, VEH data were pooled during analysis.

For analysis of multiplexed cytokine quantification, outcomes of interest included measured levels for 23 analytes grouped according to function (antiinflammatory cytokine, chemokine, pro- and antiinflammatory cytokine, proinflammatory cytokine). Each analyte was analyzed separately. A small percentage of observations in the piriform cortex (0.9%) were below the limit of detection, so those undetermined values were replaced with the lower limit of detection divided by the square root of 2. To stabilize the variance, IL-2, IL-7, GRO/KC, MIP-1a, MIP-3a, and MCP-1 were transformed with the natural log prior to analysis. Due to the repeated measures across brain regions (hippocampus and piriform cortex) for each animal, a mixed-effects regression model, including an animal-specific random effect, was used for all analyses. Factors of interest included treatment (DFP or VEH), brain region, and DPE (days 1, 3, 7, 14, and 28) and interactions between these variables were considered. Model building used the Akaike Information Criterion to choose the best model for each analyte. Contrasts were then constructed to compare treatment groups overall, or by region and/or day if any interactions were supported by the data. Wald tests were used to assess differences. To account for multiple comparisons, the Benjamini-Hochberg false discovery rate (FDR) approach was used across all p-values from the Wald tests.

Secondary analyses were run in the hippocampus only, to compare animals in the DFP and VEH groups with and without PB pretreatment. Analyses were conducted separately for each analyte. Analysis of variance was used to evaluate differences between treatment groups, either overall or by day. Akaike Information Criterion was used to identify the best model and contrasts were specified to compare DFP+PB versus DFP and VEH+PB versus VEH. There were no differences between DFP+PB and DFP or between VEH+PB and VEH. FDR was used to account for multiple comparisons across all p-values of these secondary analyses.

RESULTS

Seizures and Survival Following Acute DFP Intoxication

Acute intoxication with DFP (4 mg/kg, sc) produced severe seizure behavior, defined as a seizure severity score of ≥ 3, within 5–10 min of intoxication, consistent with previous studies (Flannery *et al.*, 2016; Pouliot *et al.*, 2016). The majority (approximately 70%) of DFP animals that exhibited seizure behavior survived until euthanized between 3 and 28 DPE. Of the surviving animals, 27 were used for imaging studies. Detailed seizure and survival data for the DFP-intoxicated animals were published previously (Hobson *et al.*, 2017; Siso *et al.*, 2017).

Establishment of Reference Region and Control Groups

In addition to regional SUV analyses of TSPO PET, SUV data were also normalized to a cerebellar reference region (SUVR), a method that may control for experimental factors such as error in the measurement of body weight (Lopresti *et al.*, 2005). The selection of the cerebellum as a reference region was based on histopathological and MRI assessments of these animals that indicated insignificant neuropathology or neuroinflammation in this brain region during the first month following acute DFP

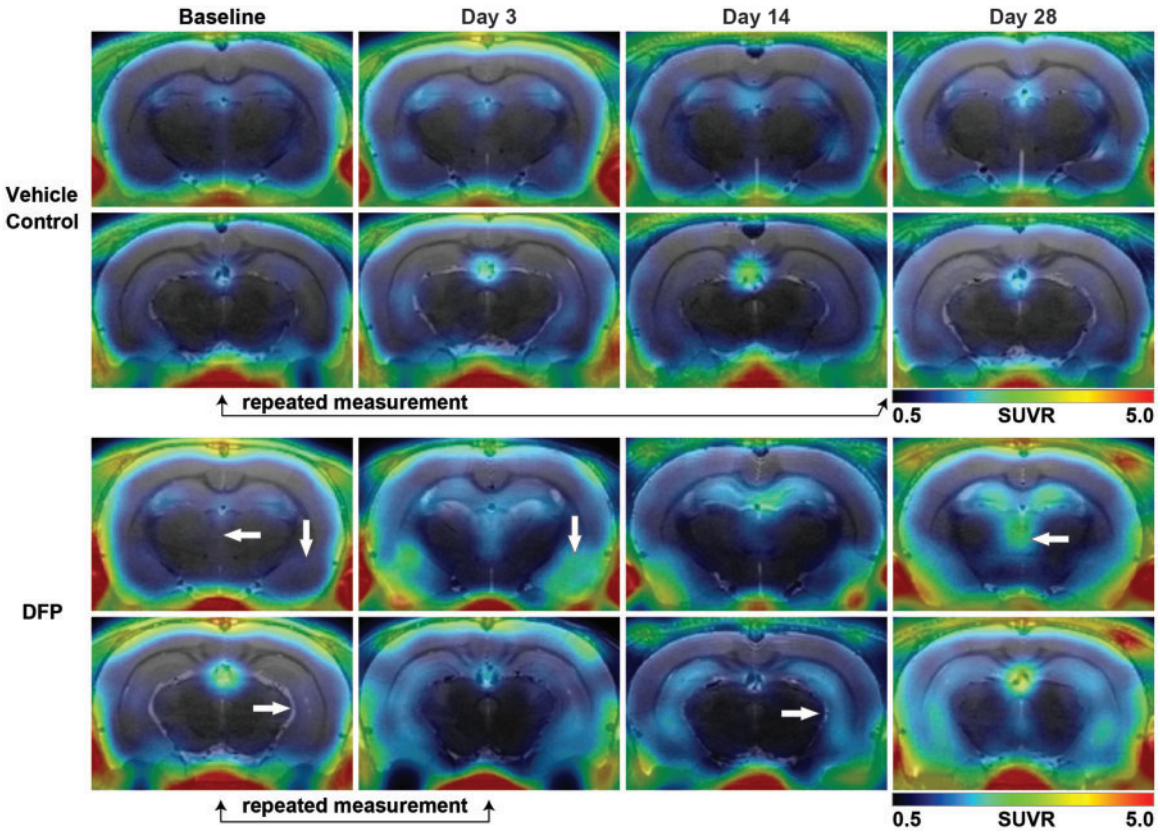

Figure 2. Acute DFP intoxication increases [^{18}F]PBR111 SUVR. Representative parametric images of [^{18}F]PBR111 SUVR in VEH (top 2 rows) and DFP-intoxicated animals (bottom 2 rows) at baseline and 3, 14, and 28 DPE. White arrows denote increased [^{18}F]PBR111 uptake in the hippocampus (arrow facing right), piriform cortex and amygdala (arrow facing downward), and thalamus (arrow facing left). Black arrows below images indicate repeated measurements of [^{18}F]PBR111 PET imaging sessions from a single VEH- or DFP-intoxicated animal, and highlight the consistency of VEH controls over the 28-day study period, and the rapid increase in TSPO labeling by [^{18}F]PBR111 during the first 3 days following acute DFP intoxication. Note: Signal penetration from outside the brain along the skull and jaw bones is predominantly due to [^{18}F] uptake in bone following defluorination of the parent tracer.

intoxication (Hobson *et al.*, 2017; Siso *et al.*, 2017). When assessed by TSPO PET, mean cerebellar SUVs of DFP-intoxicated animals on day 28 were higher than baseline and 7 DPE, but were similar at all other time points (Supplementary Table 1). A significant correlation between DPE and cerebellar SUV was detected (r_s = 0.63; 95% CI: 0.31, 0.81; $p < .001$); however, a similar trend was also observed across scans from VEH control animals ($p = .04$) (Supplementary Figure 1). Finally, there was no statistically significant correlation between cerebellar SUV and seizure severity scores ($r_s = 0.05$; 95% CI: −0.34, 0.42; $p = .81$).

TSPO PET images at baseline and following VEH exposure revealed [^{18}F]PBR111 uptake within these brains that was visually unremarkable relative to surrounding tissue and consisted of increased [^{18}F]PBR111 uptake within the ventricular system and along large blood vessels that is typical of TSPO radiotracer distribution (Bertoglio *et al.*, 2017; Walker *et al.*, 2015; Figure 2). No significant differences in [^{18}F]PBR111 uptake were observed between baseline and VEH control scans across all brain regions assessed in this study (Supplementary Table 2), and as a result, these scans were combined into a group henceforth referred to in subsequent analyses as the control group.

Acute DFP Intoxication Increases [^{18}F]PBR111 Uptake

Acute DFP intoxication produced persistent, anatomically restricted lesions in PET images characterized by areas of increased [^{18}F]PBR111 uptake in the hippocampus, piriform cortex, amygdala, and thalamus relative to the control group (Figs 2 and 3). Onset and apparent visual intensity of TSPO PET lesions varied by region with notable interanimal variation. At 3 DPE, analysis of regional SUVR revealed significant increases in [^{18}F]PBR111 within the hippocampus ($\beta = 0.74$, SE = 0.24, $p = .002$, 95% CI: 0.28, 1.21), thalamus ($\beta = 0.72$, SE = 0.25, $p = .005$, 95% CI: 0.22, 1.22), piriform cortex ($\beta = 0.46$, SE = 0.19, $p = .01$, 95% CI: 0.09, 0.83) and amygdala ($\beta = 0.66$, SE = 0.28, $p = .02$, 95% CI: 0.11, 1.21) of DFP-intoxicated animals relative to the control group (Figure 3). In contrast, analysis of regional SUV at 3 DPE yielded no significant differences in DFP-intoxicated animals compared with the control group. Beginning at 7 DPE, PET lesions in the brains of DFP-intoxicated animals appeared larger in extent compared with 3 DPE, and regional SUV metrics were significantly increased compared with the control group (SUVR and SUV, $p < .001$) and remained elevated for the duration of the study (SUVR and SUV, $p < .001$). Overall, when compared with baseline scans, there was considerable intraregional heterogeneity in SUV and SUVR measures following DFP intoxication (Figure 3).

Regional SUV and SUVR did not differ significantly between time points after DFP intoxication (Figure 3); however, the pattern of SUVR values among animals with repeat scans varied. The majority of DFP-intoxicated animals that received repeated imaging from baseline through 7 DPE demonstrated an increase in SUVR between their penultimate and final scans within that time frame (hippocampus, 5/6; thalamus, 6/6; piriform cortex, 5/6; and amygdala, 6/6) (Figure 3). In contrast, a majority of DFP-

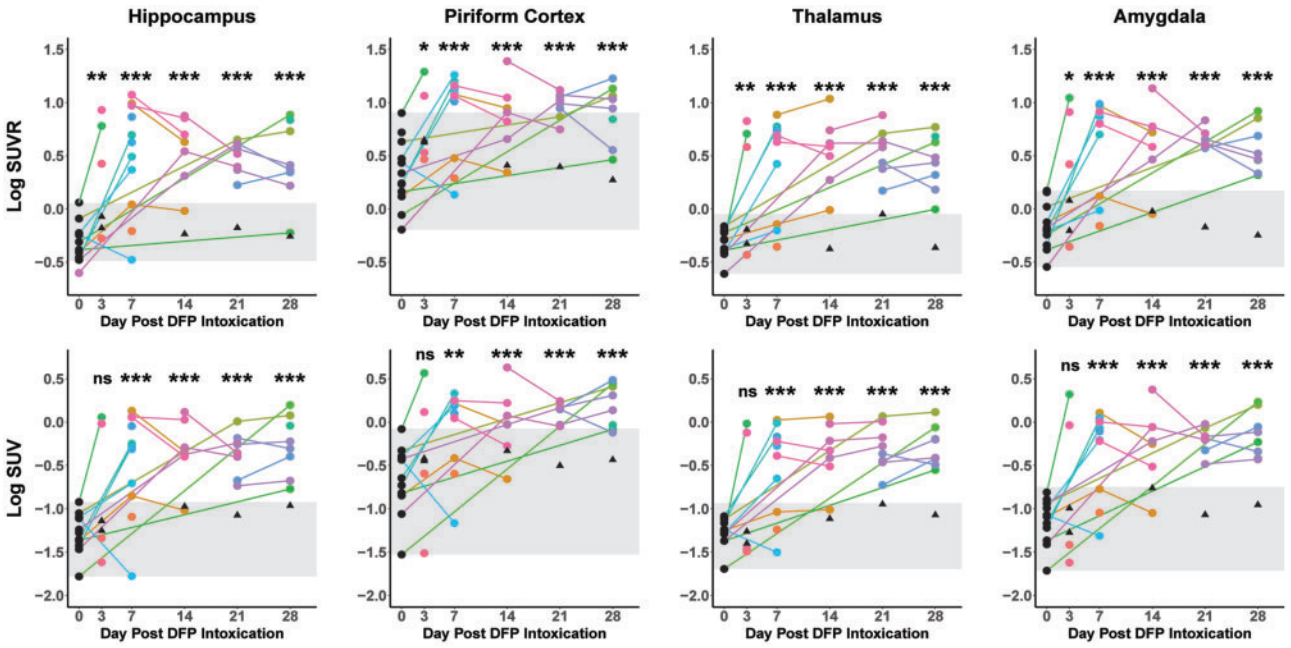

Figure 3. Temporal progression plots of mean regional [^{18}F]PBR111 SUVR and SUV in the hippocampus, piriform cortex, thalamus, and amygdala. Each data point represents a unique imaging session; lines connecting data points denote repeated measurements of a single animal. Scans of VEH controls (black triangles), animals prior to DFP or VEH intoxication (baseline scans) (black circles), and DFP-intoxicated animals (circles with unique hues per animal) are listed. Gray shading is provided for clarity and illustrates the range of the combined VEH control and baseline group. Significant increases in regional [^{18}F]PBR111 SUVR and SUV were determined using mixed-effects regression modeling to evaluate differences between DPE of DFP-intoxicated animal and the baseline + VEH control group. SUV and SUVR data (y-axes) were log transformed to better meet the assumptions of the model. All significant differences indicate increases over the baseline + VEH control group. $^{*}p < .05$, $^{**}p < .01$, and $^{***}p < .001$.

intoxicated animals with multiple repeated scans acquired 7 days or later had decreased SUVR values at their final scans when compared with their penultimate scans (hippocampus, 9/12; piriform cortex, 9/12; and amygdala, 9/12). An exception to this downward trend at later time points was noted in the thalamus, in which only 4/12 animals had lower SUVRs amongst repeated scans between 7 and 28 days.

Increases in [^{18}F]PBR111 SUV and SUVR Are Highly Correlated With Histological Markers of Neuroinflammation

Lesions defined by areas of increased SUV and SUVR corresponded spatially to regions of neuroinflammation identified by histology (Figure 4). A veterinary neuropathologist blinded to treatment evaluated regional microgliosis (identified using IBA1 immunoreactivity and scored based on number and morphology of IBA1 immunopositive cells), and astrogliosis (identified using GFAP immunoreactivity and scored based on intensity of GFAP immunofluorescence, as well as density and morphology of GFAP immunopositive cells). Gliosis was scored using a scale of 0–3, with a score of 0 referring to no microgliosis or astrogliosis, and a score of 3 corresponding to severe gliosis. Additional information is provided in the Materials and Methods section, and in a previous publication describing a detailed histopathological assessment of these animals (Siso et al., 2017). Regional measurements of SUV and SUVR collected at the final imaging time point for each animal were correlated with the corresponding histological assessment of the brain collected within 24 h of the final imaging (Table 2). SUV and SUVR were significantly correlated with scoring of microgliosis, astrogliosis, and total neuroinflammation (microgliosis + astrogliosis) across all brain regions. Overall correlation coefficients between SUVR and histology were higher than the corresponding SUV correlation coefficients in the hippocampus, thalamus, and amygdala.

Elevated Chemokine Protein Levels and Cytokine Gene Expression Corroborate Neuroinflammation Detected by TSPO PET Imaging and Histologic Assessment

To further characterize the neuroinflammation identified by TSPO PET imaging and histologic assessment, protein levels of proinflammatory (IL-6, IL-17, IL-18, M-CSF, G-CSF, GM-CSF, IFN-γ, TNF-α, IL-1α, and IL-1β), antiinflammatory (IL-4, IL-5, IL-10, and IL-13), and pleiotropic, eg, both pro- and antiinflammatory (IL-2, IL-7, IL12) cytokines, as well as chemotactic chemokines (GRO/KC, MIP-1α, MIP-3α, RANTES, VEGF, and MCP-1) were assessed by multiplex immunoassay. These data were collected from the hippocampus and piriform cortex at 1, 3, 7, 14, and 28 DPE to DFP or VEH in a cohort of animals that were not used for *in vivo* imaging and histologic assessment. Table 3 summarizes the spatiotemporal profiles of these cytokines and chemokines in DFP versus VEH animals. The temporal progression of each analyte by brain region and DPE in DFP versus VEH animals is provided in Supplementary Figs. S2–S9. Protein levels of chemotactic cytokines (GRO/KC, MIP-1α, MIP-3α, and MCP-1; $p < .001$ for each) were significantly increased in both brain regions in DFP animals at 1 DPE. Furthermore, MIP-1α and MCP-1 remained significantly elevated in DFP animals over the duration of the study (MIP-1α: $p < .003$ for days 3, 7, 14, and 28; MCP-1, hippocampus: $p < .008$ for days 3, 7, and 28; MCP-1, piriform cortex: $p < .008$ for days 3 and 7), with the exception of MCP-1 on day 14 in the piriform cortex where levels were lower ($p = .006$); there were no differences in MCP-1 on day 14 in the hippocampus ($p = .3$) or on day 28 in the piriform cortex ($p = .5$).

Generally, antiinflammatory cytokines were significantly lower in DFP compared with VEH animals over the duration of the study, particularly over the first 2 weeks postexposure. Two of the three pleiotropic (pro- and antiinflammatory) cytokines were reduced in DFP animals. All proinflammatory cytokines

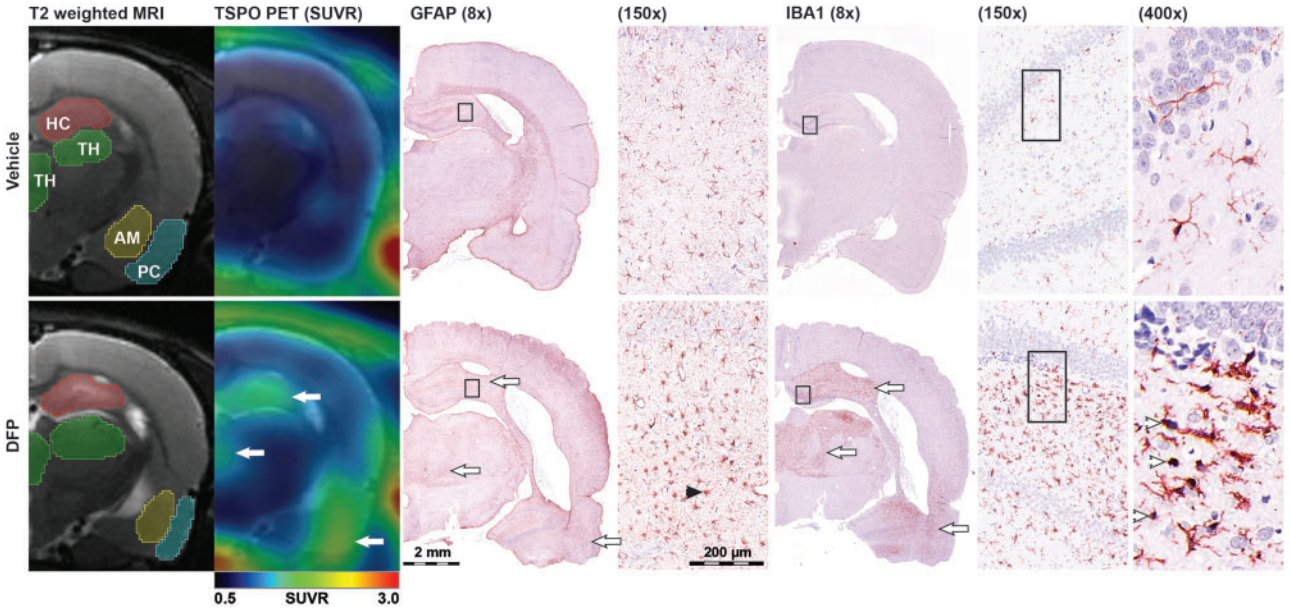

Figure 4. TSPO PET imaging corresponds spatially with immunohistochemical evidence of neuroinflammation. Images from a VEH control (top) and DFP-intoxicated animal (bottom) demonstrate spatial correspondence between areas of increased [^{18}F]PBR111 uptake and regions of severe microgliosis and astrogliosis as assessed by IBA1 and GFAP immunoreactivity respectively. The same animal analyzed by (from left to right): T_2-weighted MRI to illustrate the VOI delineation of the hippocampus (HC, red), thalamus (TH, green), amygdala (AM, yellow), and piriform cortex (PC, cyan) used to calculate the regional [^{18}F]PBR111 SUV metrics; parametric images of [^{18}F]PBR111 SUVR (color) overlaid on MRI (grayscale); composite micrographs (montaged from 20× to 400× tiled images) of GFAP (8× and 15×), and IBA1 (8×, 15×, and 400×) immunostaining. White arrows denote areas of coincident increases in [^{18}F]PBR111 SUVR, IBA1 immunoreactivity, and GFAP immunoreactivity in the hippocampus (top arrow), thalamus (middle arrow), and piriform cortex (bottom arrow) following acute DFP intoxication. Arrowheads on insets denote examples of activated microglia (white) and astrocytes (black). Note: similar inflammation is not observed in the VEH control. All panels are located approximately 4 mm bregma.

Table 2. Spearman Correlation of [^{18}F]PBR111 SUV Metrics and Histopathological Assessment of Neuroinflammation

		SUV		SUVR	
		r_s (95%CI)	*p* value	r_s (95%CI)	*p* value
Hippocampus	**IBA1**	**0.54** (0.22–0.75)	**	**0.67** (0.40–0.82)	***
	GFAP	**0.66** (0.39–0.82)	***	**0.69** (0.44–0.84)	***
	Total	**0.58** (0.27–0.77)	***	**0.68** (0.42–0.83)	***
Piriform cortex	**IBA1**	**0.69** (0.44–0.84)	***	**0.69** (0.43–0.83)	***
	GFAP	**0.58** (0.28–0.77)	***	**0.59** (0.29–0.78)	***
	Total	**0.64** (0.36–0.81)	***	**0.63** (0.34–0.80)	***
Thalamus	**IBA1**	**0.59** (0.29–0.78)	***	**0.73** (0.49–0.86)	***
	GFAP	**0.59** (0.28–0.77)	***	**0.60** (0.30–0.78)	***
	Total	**0.56** (0.24–0.76)	**	**0.64** (0.35–0.81)	***
Amygdala	**IBA1**	**0.52** (0.2–0.74)	**	**0.60** (0.30–0.78)	***
	GFAP	**0.50** (0.17–0.72)	**	**0.63** (0.35–0.80)	***
	Total	**0.52** (0.18–0.74)	**	**0.62** (0.32–0.80)	***

Abbreviations: SUV, standardized uptake value; SUVR, SUV ratio; IBA1, microgliosis assessed by ionized calcium-binding adapter molecule 1 immunoreactivity; GFAP, astrogliosis assessed by glial fibrillary acidic protein immunoreactivity, Total, sum of IBA1 and GFAP scores; r_s, Spearman correlation coefficient; 95%CI, 95 percent confidence interval.
$^{**}p < .01$, $^{***}p < .001$.

that were assessed were significantly lower in DFP animals compared with VEH in at least 1 time point.

A subset of the cytokines assessed by multiplex immunoassay was additionally quantified by qRT-PCR in the hippocampi of a small number of animals (Figure 5). These data indicate significantly increased mRNA levels of IL-1β, IL-6, IL-10, TNF-α, and IFN-γ in the hippocampi of DFP animals at early time points (1, 3, and 7 DPE).

Initial Seizure Behavior Predicts the Severity of Neuroinflammation Detected by [^{18}F]PBR111 PET

Average seizure severity over the first 4 h postDFP intoxication varied from 1.0 to 3.9 across the 27 animals imaged in this study. Animals that achieved a minimum one-time score of ≥ 3.0, suggesting induction of *status epilepticus*, but whose average seizure score was relatively lower than their peers, had less apparent uptake of [^{18}F]PBR111 in SUVR images (Figure 6A). Average seizure severity over the first 4 h was significantly, positively correlated with regional SUV and SUVR across all brain regions except the cerebellar reference (Figure 6B, Table 4). Overall, correlation coefficients between average seizure severity and regional SUVR were nominally larger than those to corresponding regional SUV.

DISCUSSION

This study is the first report of PET-based assessment of histologically validated neuroinflammation in a preclinical model of acute OP intoxication. Our findings demonstrate that TSPO PET using [^{18}F]PBR111 detects persistent, regionally-restricted, neuroinflammation in a rat model of acute DFP intoxication. Critically, the magnitude of the neuroinflammatory response, as quantified by regional SUV and SUVR, was highly correlated with neuropathologic scoring of microgliosis and astrogliosis, and seizure severity. Finally, the use of SUVR, which normalizes regional SUV mean values to a cerebellar reference region, improved correlations to both histological indices of neuroinflammation and seizure severity.

The validity of [^{18}F]PBR111-based TSPO PET imaging as a tool for monitoring neuroinflammation following acute DFP intoxication depends upon identifying a feasible method for estimating binding of a radiotracer to TSPO in the brain that correlates

Table 3. Spatiotemporal Effects of Acute DFP Intoxication on Protein Levels of Cytokines and Chemokines in the Brain

			Time Postexposure				
Cytokine Category	Cytokine	Region	Day 1	Day 3	Day 7	Day 14	Day 28
Chemotactic	MIP-1a[a]	All	↑	↑	↑	↑	↑
	MCP-1[b]	HP	↑	↑	↑	ns	↑
		PC	↑	↑	↑	↓	ns
	MIP-3a[a]	All	↑	↓	ns	ns	ns
	GRO/KC[b]	HP	↑	ns	ns	ns	ns
		PC	↑	ns	ns	↓	ns
	RANTES[c]	All			↓		
	VEGF[c]	All			↓		
Antiinflammatory	IL-4[a]	All	ns	↓	ns	↓	ns
	IL-5[a]	All	↓	↓	ns	↓	ns
	IL-10[d]	HP			↓		
		PC			ns		
	IL-13[a]	All	↓	↓	ns	↓	ns
Pleiotropic pro- and antiinflammatory	IL-2[c]	All			ns		
	IL-7[c]	All			↓		
	IL-12(p70)[c]	All			↓		
Proinflammatory	IL-1α[a]	All	ns	↓	ns	↓	ns
	IL-1β[d]	HP			↓		
		PC			ns		
	IL-6[c]	All			↓		
	IL-17[a]	All	↓	↓	ns	↓	ns
	IL-18[d]	HP			↓		
		PC			ns		
	M-CSF[c]	All			↓		
	G-CSF[a]	All	ns	↓	ns	ns	ns
	GM-CSF[c]	All			↓		
	IFN-γ[a]	All	↓	↓	ns	↓	ns
	TNF-α[d]	HP			↓		
		PC			↓		

↓ indicates levels are lower in DFP (n = 6–9 per group) compared with VEH (n = 3-4 per group), ↑ indicates levels are higher in DFP compared with VEH, and "ns" (light gray) indicates no significant difference between groups. Only differences that remained significant after an FDR correction are presented.
Abbreviations: All, pooled across brain regions; HP, hippocampus; PC, piriform cortex.
[a]Interaction between day and treatment, significant differences are presented by day.
[b]Both day by treatment and region by treatment interactions, significant differences are presented by region by day.
[c]No interactions between treatment and another factor, the global difference between DFP and VEH are presented.
[d]Interaction between region and treatment, significant differences are presented by region.

with the underlying neuropathology. SUV-based metrics are the most common analysis method for clinical PET data (Basu *et al.*, 2007). SUV can be readily calculated (equations 1 and 2) without the need for dynamic imaging, blood sampling, or input-function estimation that is required for more complex kinetic modeling and parameter estimation (Thie, 2004). The tradeoff is that SUV-based assessments are susceptible to systemic errors associated with animal-dependent parameters such as radiotracer injected dose and bodyweight. The normalization of the SUV value in a region of interest to that of a reference region, known as SUVR, has been used clinically (Lopresti *et al.*, 2005) and preclinically (Yoder *et al.*, 2011) to compensate for these sources of error; however, this process may introduce inherent biases associated with the reference region SUV measurement (Blautzik *et al.*, 2017). Despite these potential limitations, regional SUV and SUVR following acute DFP intoxication were highly correlated with the spatiotemporal pattern and magnitude of microgliosis and astrogliosis across all brain regions. We observed an unexpected correlation between SUV within the cerebellar reference region and time post-DFP intoxication, despite histological assessment indicating insignificant evidence of ongoing neuroinflammation in the cerebellum of these animals (Siso *et al.*, 2017). However, a similar upward trend in reference region SUV with increasing age was also observed in VEH animals. This subtle increase in cerebellar SUV is in line with age-related increases in TSPO expression reported within the cerebellum of Sprague Dawley rats (Walker *et al.*, 2015) that has also been reported clinically (Tuisku *et al.*, 2019). Despite this potential shortcoming of the cerebellum as a reference region, SUVR was more highly correlated with histologic assessments of neuroinflammation than SUV.

SUVR also appears more effective than SUV at reflecting the temporal progression of neuroinflammation following DFP intoxication. Mixed-model regression of regional SUV and SUVR revealed significant neuroinflammation in all brain regions of interest (hippocampus, thalamus, piriform cortex, and amygdala) from 7 to 28 DPE compared with the control group. However, SUVR additionally detected a significant increase in neuroinflammation at 3 DPE in these regions. Neuropathological assessment of these animals (Siso *et al.*, 2017), as well as previous preclinical studies of acute DFP (Flannery *et al.*, 2016; Kuruba *et al.*, 2018; Liu *et al.*, 2012; Rojas *et al.*, 2015), demonstrate robust neuroinflammation in these brain regions by 3 DPE, as defined by microgliosis, astrogliosis, and proinflammatory cytokine signaling. In addition, SUVR detection of significant neuroinflammation at 3 DPE recapitulates the results of our previous TSPO

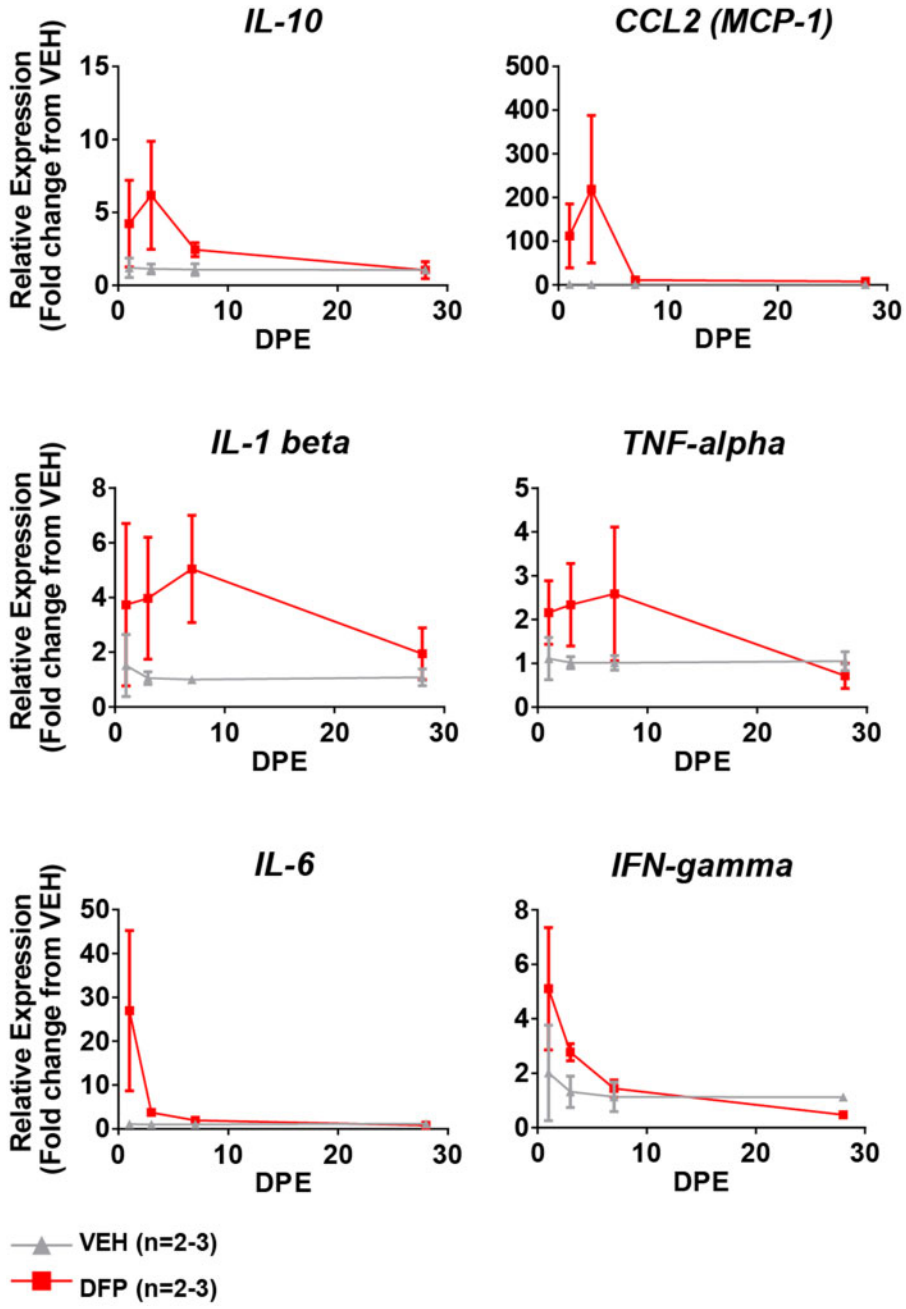

Figure 5. Changes in cytokine mRNA expression within the hippocampus as a function of time after acute DFP intoxication. qRT-PCR reveals acute, transient induction of proinflammatory (IL-1β, TNF-α, IL-6, and IFN-γ), anti-inflammatory (IL-10), and chemotactic (MCP-1) cytokine gene expression. Data presented as mean ± SE ($n = 2$–3 animals per group).

PET-based assessment of acute DFP intoxication using the first-generation radiotracer, [^{11}C]PK11195, in which significant increases in radiotracer uptake were observed as early as 2 DPE in some brain regions (Flannery *et al.*, 2016).

Seizure severity during the first few hours following DFP intoxication significantly influences the neuroinflammatory response. We identified a significant positive correlation between the SS_{AVR} during the first 4 h postDFP intoxication and SUV metrics in all brain regions except the cerebellum. This is in agreement with previous studies of acute OP intoxication in rodents demonstrating that the initial seizure severity influences the extent of neurodegeneration (Carpentier *et al.*, 2001; de Araujo Furtado *et al.*, 2010; Siso *et al.*, 2017), brain lesion size detected by MRI (Gullapalli *et al.*, 2010; Hobson *et al.*, 2017), and the development of spontaneous recurrent seizures (de Araujo Furtado *et al.*, 2010). In addition, the spatiotemporal pattern of SUV metrics observed following DFP intoxication in the rat share marked similarity to TSPO PET imaging of preclinical models of SE induced by chemicals other than OPs (Bertoglio *et al.*, 2017; Brackhan *et al.*, 2016; Dedeurwaerdere *et al.*, 2012; Yankam Njiwa *et al.*, 2017). In accordance with our findings, longitudinal TSPO PET using [^{11}C]PK11195 in a Sprague Dawley rat model of pilocarpine-induced SE revealed persistent radiotracer binding in the hippocampus, thalamus, and piriform cortex for 3 weeks

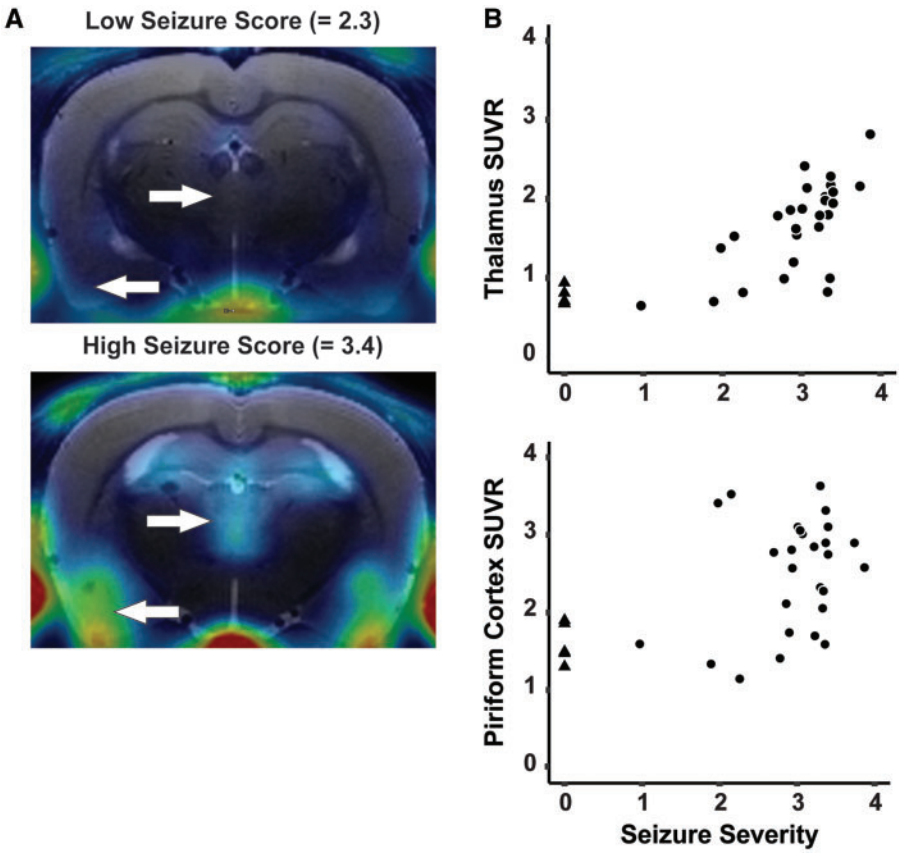

Figure 6. The extent of neuroinflammation detected by [^{18}F]PBR111 PET is highly correlated with seizure severity. A, Parametric images of SUVR from DFP-intoxicated animals with low versus high SS_{AVR} over the first 4 h postexposure. White arrows indicate differential [^{18}F]PBR111 uptake in the thalamus (arrow facing right) and the piriform cortex (arrow facing left). B, Scatter plot depicting the high positive correlation between SS_{AVR} and SUVR in the thalamus ($r_s = 0.84$; $p < .001$) and piriform cortex ($r_s = 0.48$; $p < .01$). DFP-intoxicated animals are indicated with black circles, while VEH control animals are indicated as black triangles.

Table 4. Spearman Correlations of [^{18}F]PBR111 SUV Metrics and Seizure Severity

	SUV		SUVR	
	r_s (95% CI)	p value	r_s (95% CI)	p value
Amygdala	**0.57** (0.26–0.76)	***	**0.68** (0.43–0.83)	***
Hippocampus	**0.64** (0.36–0.80)	***	**0.76** (0.55–0.87)	***
Piriform cortex	**0.45** (0.11–0.68)	**	**0.48** (0.15–0.71)	**
Thalamus	**0.70** (0.45–0.84)	***	**0.84** (0.68–0.91)	***

Abbreviations: SUV, standardized uptake value; SUVR, SUV ratio; r_s, Spearman correlation coefficient; 95%CI, 95 percent confidence interval.
**$p < .01$, ***$p < .001$.

following the initiation of seizures (Brackhan *et al.*, 2016). Corroborating our use of the cerebellum as a reference region. That study similarly reported no significant increase in radiotracer uptake within the cerebellum following SE, and utilized it as a reference region in a simplified reference tissue model-based analysis that yielded significant correlations with semi-quantitative scoring of microgliosis and astrogliosis. Another study using [^{11}C]PK11195 in a rat model of pilocarpine-induced SE concluded that SUV provided the same overall pattern of results as more complex kinetic analysis (Yankam Njiwa *et al.*, 2017). However, in contrast to our observations, significant neuroinflammation in this model was detected at 1 week, but not 1 month postSE. These differences in the duration of increased radiotracer uptake may reflect therapeutic intervention to limit SE to 90 min in the pilocarpine model, whereas in our rat model of acute DFP intoxication, seizures persisted for several hours.

The correlation between seizure severity and SUV metrics, and the pronounced similarities of TSPO PET imaging in preclinical models of acute DFP intoxication and preclinical models of SE induced by other chemicals suggest that the neuroinflammatory responses following acute DFP intoxication are determined, in large part, by the severity and/or duration of SE. It remains unclear to what extent DFP-induced neuroinflammation is triggered as a direct result of electrographic seizure activity versus a response to the neuronal cell injury and death that occurs following prolonged seizures (Siso *et al.*, 2017). Nonetheless, our data suggest that therapeutic interventions aimed at limiting the duration of OP-induced seizures may modify the magnitude and/or persistence of the neuroinflammatory response weeks after intoxication.

An ongoing debate in the field of TSPO PET imaging is whether microglia or astrocytes contribute to the TSPO PET signal. Current evidence suggests the relative contribution of these cell types may vary by disease and model system (Lavisse *et al.*, 2012; Nguyen *et al.*, 2018; Weidner *et al.*, 2018; Yamasaki *et al.*, 2017). In the rat DFP model, we observed similar correlation between SUV metrics and histopathologic scores of microgliosis and astrogliosis. Furthermore, elevated TSPO ligand binding corresponded spatially to astrogliosis and microgliosis. These observations suggest that astrogliosis and microgliosis both contribute to the TSPO PET signal in the DFP model. However,

this interpretation is somewhat inconclusive because of the low spatial resolution of preclinical PET relative to the overlapping spatial association between astrogliosis and microgliosis observed in the DFP-intoxicated brain (Siso *et al.*, 2017). To determine the relative contribution of microglia versus astrocytes to the TSPO PET signal in the rat DFP model, additional studies are needed to assess TSPO expression at the cellular rather than regional level.

To further characterize DFP-induced neuroinflammation, we evaluated cytokine and chemokine expression at both the protein and mRNA level. Consistent with a recently published study of the rat DFP model that quantified mRNA levels of cytokines at 24 h postexposure (Liang *et al.*, 2018), we observed increased transcription of pro-, antiinflammatory, and chemotactic cytokines and chemokines at early time points in the DFP versus VEH brain. DFP intoxication also caused early and persistent elevation of chemokines at the protein level. These data corroborated DFP-induced neuroinflammatory responses detected by TSPO PET and histopathology. The persistent elevated chemokine levels could explain the large numbers of myeloid cells observed in the brain 1 month postDFP intoxication (Siso *et al.*, 2017).

In contrast, protein levels of nearly all pro- and antiinflammatory cytokines were decreased in the brain of DFP animals at all-time points examined. One explanation for the discrepancy between mRNA and protein levels of these cytokines is suggested by observations from a rat model of acute soman intoxication that protein levels of many cytokines peak within the first several hours and return to baseline by 24–48 h postexposure (Johnson and Kan, 2010). We may have missed the window of increased protein levels of cytokines in the DFP rat. However, data generated using a rat model of acute sarin intoxication indicate reduced levels in IL-10, IL-6, and IL-1β protein coincident with significantly increased TSPO radiobinding_at 5 weeks postintoxication (Chapman *et al.*, 2015). Interestingly, these data were in contrast to a previous study of this same model by the same laboratory in which increased cytokine levels were detected following sarin exposure (Chapman *et al.*, 2006). A notable difference between the 2 studies was the extent of morbidity (increased mortality in the 2015 vs 2006 publication). The authors hypothesized that OP-intoxicated animals with severe pathology have reduced cytokine levels due to death of cytokine producing cells. We observed 24% mortality in the DFP-intoxicated animals used in this study, and histopathologic assessment of surviving DFP animals revealed areas of pan necrosis, extensive cystic lesions with tissue liquefaction, and tissue calcification (Siso, 2017), which is similar to reports of severe sarin-induced neuropathology (Kadar *et al.*, 1995). Overall, there is a general lack of consensus regarding the temporal progression of cytokine levels following acute OP intoxication (Banks and Lein, 2012; Chapman *et al.*, 2006, 2015; Johnson *et al.*, 2011; Johnson and Kan, 2010; Liang *et al.*, 2018). The available data suggest discrepancies between studies reflect differences in the OP and dose used in the study, seizure severity, extent of neuropathology, time postexposure, and method of quantification.

Overall, the temporal progression of neuroinflammation we observed in the rat DFP model using multiple approaches is consistent with the pattern of progressive neurodegeneration observed in preclinical models of acute OP intoxication (Collombet, 2011; Siso *et al.*, 2017). Furthermore, this neuroinflammation precedes and overlaps temporally with the development of recurrent seizures and behavioral deficits reported in these models (de Araujo Furtado *et al.*, 2010; Flannery *et al.*, 2016; Rojas *et al.*, 2018). Collectively, these observations support the hypothesis that neuroinflammation influences the development of persistent neurological consequences following acute OP intoxication. The persistence of similarly elevated SUV metrics across the 28-day time course of the current study suggests that therapeutic windows for modifying OP-induced neuroinflammatory responses may extend beyond the initial seizure period.

In conclusion, these results establish SUV-based analysis of [^{18}F]PBR111 PET as a robust, noninvasive method for longitudinal monitoring of microgliosis and astrogliosis in preclinical models of acute OP intoxication. SUVR appeared superior to SUV alone; normalization of SUV to a cerebellar reference region enabled earlier detection of neuroinflammatory responses and improved correlation with underlying neuropathology. Additional studies that integrate full kinetic modeling of [^{18}F]PBR111 PET data from the DFP rat model are needed to fully understand the value of SUV metrics in relation to more sensitive, but labor intensive, binding estimation approaches for monitoring neuroinflammation. The interanimal variability in neuroinflammation following acute DFP intoxication in this study, a common characteristic of preclinical models of acute OP intoxication (Gullapalli *et al.*, 2010), highlight the important role *in vivo* imaging can serve in accounting for biological variation during costly and time-consuming studies, such as long-term behavioral studies and evaluation of candidate therapies.

SUPPLEMENTARY DATA

Supplementary data are available at *Toxicological Sciences* online.

DECLARATION OF CONFLICTING INTERESTS

The authors declared no potential conflicts of interest with respect to the research, authorship, and/or publication of this article.

ACKNOWLEDGMENTS

The authors gratefully thank Jennifer Fung and Charles Smith (UC Davis Center for Molecular and Genomic Imaging) for their assistance with animal care and imaging, Dave Kukis and Lina Planutyte (UC Davis Center for Molecular and Genomic Imaging) for assistance with radiotracer synthesis, and Dr Simon Cherry (UC Davis) for advice on experimental design. The authors also thank Dr. Andrew Katsifis (Royal Prince Alfred Hospital, Syndney, Australia) for kindly providing precursor and standard material for the synthesis of [^{18}F]PBR111.

FUNDING

This work was supported by the CounterACT Program, National Institutes of Health Office of the Director and the National Institute of Neurological Disorders and Stroke (U54 NS079202 to P.J.L.), the National Institute of General Medical Sciences (T32 GM099608 to B.A.H.), the David and Dana Loury Foundation (predoctoral fellowship to B.A.H.), and the ARCS Foundation (predoctoral fellowship to B.A.H.).

REFERENCES

Aroniadou-Anderjaska, V., Figueiredo, T. H., Apland, J. P., Prager, E. M., Pidoplichko, V. I., Miller, S. L., and Braga, M. F. (2016). Long-term neuropathological and behavioral impairments after exposure to nerve agents. *Ann. N. Y. Acad. Sci.* **1374**, 17–28.

Banks, C. N., and Lein, P. J. (2012). A review of experimental evidence linking neurotoxic organophosphorus compounds and inflammation. *Neurotoxicology* **33**, 575–584.

Basu, S., Zaidi, H., Houseni, M., Bural, G., Udupa, J., Acton, P., Torigian, D. A., and Alavi, A. (2007). Novel quantitative techniques for assessing regional and global function and structure based on modern imaging modalities: Implications for normal variation, aging and diseased states. *Semin. Nucl. Med.* **37**, 223–239.

Bertoglio, D., Verhaeghe, J., Santermans, E., Amhaoul, H., Jonckers, E., Wyffels, L., Van Der Linden, A., Hens, N., Staelens, S., and Dedeurwaerdere, S. (2017). Non-invasive PET imaging of brain inflammation at disease onset predicts spontaneous recurrent seizures and reflects comorbidities. *Brain Behav. Immun.* **61**, 69–79.

Betlazar, C., Harrison-Brown, M., Middleton, R. J., Banati, R., and Liu, G. J. (2018). Cellular sources and regional variations in the expression of the neuroinflammatory marker translocator protein (TSPO) in the normal brain. *Int. J. Mol. Sci.* **19**,

Blautzik, J., Brendel, M., Sauerbeck, J., Kotz, S., Scheiwein, F., Bartenstein, P., Seibyl, J., Rominger, A., and Alzheimer's Disease Neuroimaging, I. (2017). Reference region selection and the association between the rate of amyloid accumulation over time and the baseline amyloid burden. *Eur. J. Nucl. Med. Mol. Imaging* **44**, 1364–1374.

Bonsack, F., and Sukumari-Ramesh, S. (2018). TSPO: An evolutionarily conserved protein with elusive functions. *Int. J. Mol. Sci.* **19**(6), pii:E1694.

Bourdier, T., Pham, T. Q., Henderson, D., Jackson, T., Lam, P., Izard, M., and Katsifis, A. (2012). Automated radiosynthesis of [^{18}F]PBR111 and [^{18}F]PBR102 using the Tracerlab FXFN and Tracerlab MXFDG module for imaging the peripheral benzodiazepine receptor with PET. *Appl Radiat Isot* **70**, 176–83.

Brackhan, M., Bascunana, P., Postema, J. M., Ross, T. L., Bengel, F. M., Bankstahl, M., and Bankstahl, J. P. (2016). Serial quantitative TSPO-targeted PET reveals peak microglial activation up to 2 weeks after an epileptogenic brain insult. *J. Nucl. Med.* **57**, 1302–1308.

Bruun, D. A., Guignet, M., Harvey, D. J., and Lein, P. J. (2019). Pretreatment with pyridostigmine bromide has no effect on seizure behavior or 24 hour survival in the rat model of acute diisopropylfluorophosphate intoxication. *NeuroToxicol.* **73**, 81–84.

Carpentier, P., Foquin, A., Kamenka, J. M., Rondouin, G., Lerner-Natoli, M., de Groot, D. M., and Lallement, G. (2001). Effects of thienylphencyclidine (TCP) on seizure activity and brain damage produced by soman in guinea-pigs: ECoG correlates of neurotoxicity. *Neurotoxicology* **22**, 13–28.

Chapman, S., Kadar, T., and Gilat, E. (2006). Seizure duration following sarin exposure affects neuro-inflammatory markers in the rat brain. *Neurotoxicology* **27**, 277–283.

Chapman, S., Yaakov, G., Egoz, I., Rabinovitz, I., Raveh, L., Kadar, T., Gilat, E., and Grauer, E. (2015). Sarin-induced brain damage in rats is attenuated by delayed administration of midazolam. *Neurotoxicology* **49**, 132–138.

Chen, Y. (2012). Organophosphate-induced brain damage: Mechanisms, neuropsychiatric and neurological consequences, and potential therapeutic strategies. *Neurotoxicology* **33**, 391–400.

Collombet, J. M. (2011). Nerve agent intoxication: Recent neuropathophysiological findings and subsequent impact on medical management prospects. *Toxicol. Appl. Pharmacol.* **255**, 229–241.

Collombet, J. M., Four, E., Bernabe, D., Masqueliez, C., Burckhart, M. F., Baille, V., Baubichon, D., and Lallement, G. (2005). Soman poisoning increases neural progenitor proliferation and induces long-term glial activation in mouse brain. *Toxicology* **208**, 319–334.

de Araujo Furtado, M., Lumley, L. A., Robison, C., Tong, L. C., Lichtenstein, S., and Yourick, D. L. (2010). Spontaneous recurrent seizures after status epilepticus induced by soman in Sprague-Dawley rats. *Epilepsia* **51**, 1503–1510.

de Araujo Furtado, M., Rossetti, F., Chanda, S., and Yourick, D. (2012). Exposure to nerve agents: From status epilepticus to neuroinflammation, brain damage, neurogenesis and epilepsy. *Neurotoxicology* **33**, 1476–1490.

Dedeurwaerdere, S., Callaghan, P. D., Pham, T., Rahardjo, G. L., Amhaoul, H., Berghofer, P., Quinlivan, M., Mattner, F., Loc'h, C., Katsifis, A., *et al.* (2012). PET imaging of brain inflammation during early epileptogenesis in a rat model of temporal lobe epilepsy. *EJNMMI Res.* **2**, 60.

Deshpande, L. S., Carter, D. S., Blair, R. E., and DeLorenzo, R. J. (2010). Development of a prolonged calcium plateau in hippocampal neurons in rats surviving status epilepticus induced by the organophosphate diisopropylfluorophosphate. *Toxicol. Sci.* **116**, 623–631.

Dupont, A. C., Largeau, B., Santiago Ribeiro, M. J., Guilloteau, D., Tronel, C., and Arlicot, N. (2017). Translocator protein-18 kDa (TSPO) positron emission tomography (PET) imaging and its clinical impact in neurodegenerative diseases. *Int. J. Mol. Sci.* **18**(4), pii: E785.

Ferrara-Bowens, T. M., Chandler, J. K., Guignet, M. A., Irwin, J. F., Laitipaya, K., Palmer, D. D., Shumway, L. J., Tucker, L. B., McCabe, J. T., Wegner, M. D., *et al.* (2017). Neuropathological and behavioral sequelae in IL-1R1 and IL-1Ra gene knockout mice after soman (GD) exposure. *Neurotoxicology* **63**, 43–56.

Flannery, B. M., Bruun, D. A., Rowland, D. J., Banks, C. N., Austin, A. T., Kukis, D. L., Li, Y., Ford, B. D., Tancredi, D. J., Silverman, J. L., *et al.* (2016). Persistent neuroinflammation and cognitive impairment in a rat model of acute diisopropylfluorophosphate intoxication. *J. Neuroinflammation* **13**, 267.

Fookes, C. J. R., Pham, T. Q., Mattner, F., Greguric, I., Loc'h, C., Liu, X., Berghofer, P., Shepherd, R., Gregoire, M.-C., and Katsifis, A. (2008). Synthesis and biological evaluation of substituted [18F]imidazo[1, 2-a]pyridines and [18F]pyrazolo[1, 5-a]pyrimidines for the study of the peripheral benzodiazepine receptor using positron emission tomography. *J. Med. Chem.* **51**, 3700–3712.

Guignet, M., and Lein, P. J. (2019). Organophosphates. In *Advances in Neurotoxicology: Role of Inflammation in Environmental Neurotoxicity* (M. Aschner, and L. G. Costa, Eds.), Vol. **3**, pp. 35–79. Academic Press, Cambridge, MA.

Guilarte, T. R. (2018). TSPO in diverse CNS pathologies and psychiatric disease: A critical review and a way forward. *Pharmacol. Ther.* **194**, 44–58.

Gullapalli, R. P., Aracava, Y., Zhuo, J., Helal Neto, E., Wang, J., Makris, G., Merchenthaler, I., Pereira, E. F., and Albuquerque, E. X. (2010). Magnetic resonance imaging reveals that

galantamine prevents structural brain damage induced by an acute exposure of guinea pigs to soman. *Neurotoxicology* **31**, 67–76.

Gunnell, D., Eddleston, M., Phillips, M. R., and Konradsen, F. (2007). The global distribution of fatal pesticide self-poisoning: Systematic review. *BMC Public Health* **7**, 357.

Hobson, B. A., Siso, S., Rowland, D. J., Harvey, D. J., Bruun, D. A., Garbow, J. R., and Lein, P. J. (2017). From the cover: Magnetic resonance imaging reveals progressive brain injury in rats acutely intoxicated with diisopropylfluorophosphate. *Toxicol. Sci.* **157**, 342–353.

Johnson, E. A., Dao, T. L., Guignet, M. A., Geddes, C. E., Koemeter-Cox, A. I., and Kan, R. K. (2011). Increased expression of the chemokines CXCL1 and MIP-1alpha by resident brain cells precedes neutrophil infiltration in the brain following prolonged soman-induced status epilepticus in rats. *J. Neuroinflammation* **8**, 41.

Johnson, E. A., and Kan, R. K. (2010). The acute phase response and soman-induced status epilepticus: Temporal, regional and cellular changes in rat brain cytokine concentrations. *J. Neuroinflammation* **7**, 40.

Kadar, T., Shapira, S., Cohen, G., Sahar, R., Alkalay, D., and Raveh, L. (1995). Sarin-induced neuropathology in rats. *Hum. Exp. Toxicol.* **14**, 252–259.

Kim, Y. B., Hur, G. H., Shin, S., Sok, D. E., Kang, J. K., and Lee, Y. S. (1999). Organophosphate-induced brain injuries: Delayed apoptosis mediated by nitric oxide. *Environ. Toxicol. Pharmacol.* **7**, 147–152.

Kuruba, R., Wu, X., and Reddy, D. S. (2018). Benzodiazepine-refractory status epilepticus, neuroinflammation, and interneuron neurodegeneration after acute organophosphate intoxication. *Biochim. Biophys. Acta* **1864**, 2845–2858.

Lavisse, S., Guillermier, M., Herard, A. S., Petit, F., Delahaye, M., Van Camp, N., Ben Haim, L., Lebon, V., Remy, P., Dolle, F., *et al.* (2012). Reactive astrocytes overexpress TSPO and are detected by TSPO positron emission tomography imaging. *J. Neurosci.* **32**, 10809–10818.

Liang, L. P., Pearson-Smith, J. N., Huang, J., McElroy, P., Day, B. J., and Patel, M. (2018). Neuroprotective effects of AEOL10150 in a rat organophosphate model. *Toxicol. Sci.* **162**, 611–621.

Liu, C., Li, Y., Lein, P. J., and Ford, B. D. (2012). Spatiotemporal patterns of GFAP upregulation in rat brain following acute intoxication with diisopropylfluorophosphate (DFP). *Curr. Neurobiol.* **3**, 90–97.

Lopresti, B. J., Klunk, W. E., Mathis, C. A., Hoge, J. A., Ziolko, S. K., Lu, X., Meltzer, C. C., Schimmel, K., Tsopelas, N. D., DeKosky, S. T., *et al.* (2005). Simplified quantification of Pittsburgh Compound B amyloid imaging PET studies: A comparative analysis. *J. Nucl. Med.* **46**, 1959–1972.

Mew, E. J., Padmanathan, P., Konradsen, F., Eddleston, M., Chang, S. S., Phillips, M. R., and Gunnell, D. (2017). The global burden of fatal self-poisoning with pesticides 2006-15: Systematic review. *J. Affect. Disord.* **219**, 93–104.

Nguyen, D. L., Wimberley, C., Truillet, C., Jego, B., Caille, F., Pottier, G., Boisgard, R., Buvat, I., and Bouilleret, V. (2018). Longitudinal positron emission tomography imaging of glial cell activation in a mouse model of mesial temporal lobe epilepsy: Toward identification of optimal treatment windows. *Epilepsia* **59**, 1234–1244.

Owen, D. R., and Matthews, P. M. (2011). Imaging brain microglial activation using positron emission tomography and translocator protein-specific radioligands. *Int. Rev. Neurobiol.* **101**, 19–39.

Paxinos, G., and Watson, C. (2007). *The Rat Brain in Stereotaxic Coordinates*. 6th ed. Academic Press/Elsevier, Amsterdam; Boston.

Pereira, E. F., Aracava, Y., DeTolla, L. J., Jr, Beecham, E. J., Basinger, G. W., Jr, Wakayama, E. J., and Albuquerque, E. X. (2014). Animal models that best reproduce the clinical manifestations of human intoxication with organophosphorus compounds. *J. Pharmacol. Exp. Ther.* **350**, 313–321.

Perry, V. H., Nicoll, J. A., and Holmes, C. (2010). Microglia in neurodegenerative disease. *Nat. Rev. Neurol.* **6**, 193–201.

Pfaffl, M. W., Horgan, G. W., and Dempfle, L. (2002). Relative expression software tool (REST) for group-wise comparison and statistical analysis of relative expression results in real-time PCR. *Nucleic Acids Res.* **30**, e36.

Pouliot, W., Bealer, S. L., Roach, B., and Dudek, F. E. (2016). A rodent model of human organophosphate exposure producing status epilepticus and neuropathology. *Neurotoxicology* **56**, 196–203.

Rojas, A., Ganesh, T., Lelutiu, N., Gueorguieva, P., and Dingledine, R. (2015). Inhibition of the prostaglandin EP2 receptor is neuroprotective and accelerates functional recovery in a rat model of organophosphorus induced status epilepticus. *Neuropharmacology* **93**, 15–27.

Rojas, A., Ganesh, T., Manji, Z., O'Neill, T., and Dingledine, R. (2016). Inhibition of the prostaglandin E2 receptor EP2 prevents status epilepticus-induced deficits in the novel object recognition task in rats. *Neuropharmacology* **110(Pt A)**, 419–430.

Rojas, A., Wang, W., Glover, A., Manji, Z., Fu, Y., and Dingledine, R. (2018). Beneficial outcome of urethane treatment following status epilepticus in a rat organophosphorus toxicity model. *eNeuro* **5**, ENEURO.0070-18.2018.

Siso, S., Hobson, B. A., Harvey, D. J., Bruun, D. A., Rowland, D. J., Garbow, J. R., and Lein, P. J. (2017). Spatiotemporal progression and remission of lesions in the rat brain following acute intoxication with diisopropylfluorophosphate. *Toxicol. Sci.* **157**, 330–341.

Spradling, K. D., Lumley, L. A., Robison, C. L., Meyerhoff, J. L., and Dillman, J. F. 3rd. (2011). Transcriptional responses of the nerve agent-sensitive brain regions amygdala, hippocampus, piriform cortex, septum, and thalamus following exposure to the organophosphonate anticholinesterase sarin. *J. Neuroinflammation* **8**, 84.

Stamou, M., Wu, X., Kania-Korwel, I., Lehmler, H. J., and Lein, P. J. (2014). Cytochrome p450 mRNA expression in the rodent brain: Species-, sex-, and region-dependent differences. *Drug Metab. Dispos.* **42**, 239–244.

Thie, J. A. (2004). Understanding the standardized uptake value, its methods, and implications for usage. *J. Nucl. Med.* **45**, 1431–1434.

Tuisku, J., Plaven-Sigray, P., Gaiser, E. C., Airas, L., Al-Abdulrasul, H., Bruck, A., Carson, R. E., Chen, M.-K., Cosgrove, K. P., Ekblad, L., *et al.* (2019). Effects of age, BMI and sex on the glial cell marker TSPO - A multicentre [11C]PBR28 HRRT PET study. *bioRxiv*.

Van Camp, N., Boisgard, R., Kuhnast, B., Theze, B., Viel, T., Gregoire, M. C., Chauveau, F., Boutin, H., Katsifis, A., Dolle, F., *et al.* (2010). In vivo imaging of neuroinflammation: A comparative study between [(18)F]PBR111, [(11)C]CLINME and [(11)C]PK11195 in an acute rodent model. *Eur. J. Nucl. Med. Mol. Imaging* **37**, 962–972.

Vivash, L., and O'Brien, T. J. (2016). Imaging microglial activation with TSPO PET: Lighting up neurologic diseases? *J. Nucl. Med.* **57**, 165–168.

Walker, M. D., Dinelle, K., Kornelsen, R., Lee, N. V., Miao, Q., Adam, M., Takhar, C., Mak, E., Schulzer, M., Farrer, M. J., *et al.* (2015). [11C]PBR28 PET imaging is sensitive to neuroinflammation in the aged rat. *J. Cereb. Blood Flow Metab.* **35**, 1331–1338.

Weidner, L. D., Kannan, P., Mitsios, N., Kang, S. J., Hall, M. D., Theodore, W. H., Innis, R. B., and Mulder, J. (2018). The expression of inflammatory markers and their potential influence on efflux transporters in drug-resistant mesial temporal lobe epilepsy tissue. *Epilepsia* **59**, 1507–1517.

Yamasaki, T., Fujinaga, M., Mori, W., Zhang, Y., Wakizaka, H., Nengaki, N., Xie, L., Hatori, A., and Zhang, M. R. (2017). In vivo monitoring for regional changes of metabotropic glutamate receptor subtype 1 (mGluR1) in pilocarpine-induced epileptic rat brain by small-animal PET. *Sci. Rep.* **7**, 14945.

Yankam Njiwa, J., Costes, N., Bouillot, C., Bouvard, S., Fieux, S., Becker, G., Levigoureux, E., Kocevar, G., Stamile, C., Langlois, J. B., *et al.* (2017). Quantitative longitudinal imaging of activated microglia as a marker of inflammation in the pilocarpine rat model of epilepsy using [(11)C]- (R)-PK11195 PET and MRI. *J. Cereb. Blood Flow Metab.* **37**, 1251–1263.

Yoder, K. K., Mock, B. H., Zheng, Q. H., McCarthy, B. P., Riley, A. A., and Hutchins, G. D. (2011). Assessment of i.p. injection of [18F]fallypride for behavioral neuroimaging in rats. *J. Neurosci. Methods* **196**, 70–75.